Journal of Forestry Research (2009) 20(3): 199−204
DOI 10.1007/s11676-009-0039-6

RESEARCH PAPER

Effects of windbreak width in wind direction on wind velocity reduction

Mulati Yusaiyin, Norio Tanaka*

Graduate School of Science and Engineering, Saitama University, 255 Shimo-okubo, Sakura-ku, Saitama, Saitama, 338-8570, Japan

Abstract: The variations of drag force acting on the windbreak and the bulk drag coefficients for different windbreak widths were studied experimentally in the Eiffel-type non-circulating wind tunnel at the Hydraulic Engineering Laboratory, Saitama University, Japan, to elucidate the effects of windbreak width in the wind direction on wind velocity reduction behind a windbreak. The variations of flow field for different windbreak widths were studied numerically by using the two-dimensional Reynolds-averaged Navier-Stokes (RANS) equation with a k-ε turbulence closure model. Results show that the total drag force to wind increased with increasing windbreak width, but the bulk drag coefficient decreased slightly. The relationship between the bulk drag coefficient C_d and the windbreak width W and height H can be presented by the equation of $C_d=k_d\,(W/H)^{-b}$ (k_d, b: constants). The result of the numerical simulation shows that the windbreak width greatly affects the location and the value of the minimum wind velocity. The wind velocity decreased by 15%–22% as the windbreak width increased.

Keywords: drag force; drag coefficient; k-ε model; numerical simulation; optical porosity

Introduction

Windbreaks have been used for centuries to modify wind profiles and to defend against wind damage. In the last few decades, systematic studies have been considered to determine the effects of windbreaks on wind velocity reduction. The commonly used descriptor of the internal structure of an artificial windbreak has been ‘optical porosity,’ which is defined as the ratio between the open area of the windbreak and its total area. Numerous experiments have been conducted with very thin artificial fences or screens in laboratory wind tunnels (e.g. Moysey and McPherson 1966; Raine and Stevenson 1977; Perera 1981) and in field experiments (e.g., Bradley and Mulhearn1983; Wilson 1987). The flow field around windbreaks has also been analyzed by numerical simulations (Hagen et al. 1981; Wilson 1985; Wang and Takle 1995). Most recently, Cornelis and Gabrieis (2005) measured the total wind velocity reduction coefficient (1-velocity disturbed by the windbreak/velocity in the absence of windbreak) of windbreaks with optical porosities (m^2/m^2) ranging from 0.0 to 1.0, and concluded that a porosity of 0.20–0.35 is optimal in terms of wind velocity reduction considering one, two and three rows of windbreak. Thus, the wind velocity reduction effects of artificial fences and screens, including the function of windbreak porosity, are well understood.

Under natural conditions, a windbreak forest with a certain width will produce aerodynamic effects when wind flows across it, distinctly different from that of an artificial wind fence does. For thin artificial windbreaks, the porosity is equivalent to the optical porosity. For wide natural windbreaks, optical porosity is not always the appropriate parameter for expressing the optimal condition because optical porosity shows only the two-dimensional gap (ratio between open area and total area) rather than the three-dimensional spaces (volumetric porosity) through which the wind flows across the width of the windbreak. Nevertheless, optical porosity has frequently served as a descriptor of natural windbreaks for lack of a practical alternative (Heisler and DeWalle 1988). Therefore, most previous studies used the drag coefficient for narrow artificial windbreaks (e.g., Woodruff et al. 1963; Seginer 1972; Guyot 1978) or measured the drag coefficient directly by conducting wind-tunnel experiments on simulated models of narrow and realistic windbreaks with different optical porosities (Guan et al. 2003). Only Wang and Takle (1996) reported a set of numerical experiments using a model system with a fixed porosity windbreak to study the effects of three dimensionality of the windbreak structure. The result showed that the total drag force of the entire windbreak varies little with the changes in windbreak width and structure. However, windbreak width greatly affects the location of the minimum wind velocity, pressure perturbation, and permeability of the windbreak.

The main goal of windbreak design is to find the optimum windbreak width that minimizes the loss of land, decreases the

---

Received: 2009-03-16; Accepted: 2009-04-14

Biography: Mulati Yusaiyin, Male (1968-), Ph.D. student, Graduate School of Science and Engineering, Saitama University, 255 Shimo-okubo, Sakura-ku, Saitama, Saitama, 338-8570, Japan.
E-mail: murath68@yahoo.com
*Corresponding author: E-mail: tanaka01@mail.saitama-u.ac.jp
Responsible editor: Hu Yanbo

cost of planting and maintaining, and yields the optimum protection of adjacent areas (Wang and Takle 1996). Therefore, the objective of this investigation was to study the effects of windbreak width on wind velocity reduction. The relationship between the drag coefficient and windbreak width was determined by wind tunnel experiments. In addition, the wind flow around windbreaks with different widths was also studied using a numerical simulation.

Materials and methods

Simulation of surface boundary layer

Experiments were conducted in the Eiffel-type non-circulating wind tunnel at the Hydraulic Engineering Laboratory, Saitama University, Japan (Fig. 1). The wind tunnel has a total length of 11.3 m, and a working section length of 5.0 m with a cross-sectional area of 0.5 m width and 0.5 m height. To simulate the surface boundary layer, a layer of gravel (diameter = 2–3 cm) was uniformly spread on the floor of the first section (length = 1.0 m) to increase the surface friction and a mean flow velocity U_0= 10 m/s was used. The wind profile in the surface boundary layer was arranged according to the well-known logarithmic function that can be expressed as:

$$u_z = \frac{u_*}{\kappa} \ln \frac{z}{z_0} \tag{1}$$

where u_z is the wind velocity at height z, u_* is the friction velocity, κ (=0.4) is the von Karman constant, and z_0 is the surface roughness length.

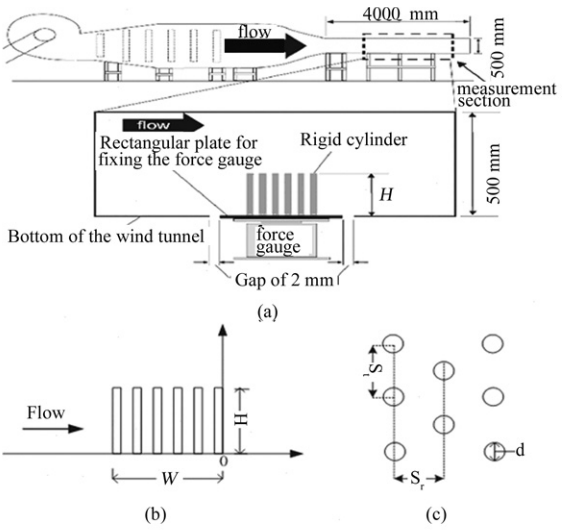

Fig. 1 Schematic of vegetation model used in experiments: (a) experimental apparatus, (b) side view, (c) details of vegetation arrangement (plan view)

The friction velocity u_* and the surface roughness length z_0 were estimated from the measurements using equation (1). The roughness and friction velocity were 0.002 m and 0.46 m/s, respectively. The boundary layer thickness was 0.10–0.12 m. The fluid properties of the simulation should match the turbulent field conditions; this can be quantified by the Reynolds number R_e as:

$$R_e = \frac{uL}{\nu} \tag{2}$$

where L is the characteristic length (m) (the average of the width and height of the wind tunnel working section), u is the mean wind velocity, and v is the kinematic viscosity.

For rectangular pipe, a turbulent regime occurs at Reynolds numbers higher than 1 400 (Bagnold 1973). According to this value, the flow in our wind tunnel was always fully turbulent at velocities greater than 0.049 m/s. Furthermore, the study of scaled windbreaks requires that this factor of the wind tunnel equals the full-scale factor (Jenson 1958), hence:

$$\left(\frac{H}{z_0}\right)_w = \left(\frac{H}{z_0}\right)_f \tag{3}$$

where H is the windbreak height (m), and subscripts w and f denote the wind tunnel and the full-scale conditions, respectively. In this study, H/z_0 was set at 500.

Drag force measurement

In principle, a windbreak exerts a drag force on the wind field, causing net losses of momentum in the incompressible airflow; thus, the frontal part of the windbreak reduces the drag force on the rear side of the windbreak (sheltering effect) (Raine and Stevenson 1977). Although there have been many studies of this sheltering effect, most of them investigated thin artificial windbreaks and studied the relationship between the optical porosity of the windbreak and the drag coefficients. The relationships between the drag coefficient and windbreak width have not been reported in previous studies. Therefore, we directly measured the drag force that changes with windbreak width. A two-axis load cell (with stream-wise (X) and transverse (Y) directions, type LB-60, SSK Co., Ltd.) that has a resolution of 1/1000 and can measure a maximum load of 1.0 Newtons was used to measure the drag force on the windbreak model. The drag force per fluid mass due to vegetation may be described, as mentioned by Nepf (1999), as:

$$F = \left[\frac{\text{force}}{\text{mass}}\right] = \frac{1}{2} C_d a U^2 \tag{4}$$

where F is the drag force per fluid mass (N), and C_d is the bulk drag coefficient, ρ is the fluid density (kg/m^3), U is the equivalent uniform velocity (m/s), and a is the projected plant area unit volume (m^2/m^3). If the plants are modeled as cylinders,

$$a = Nd = \frac{dH}{\Delta S^2 H} = \frac{d}{\Delta S^2} \tag{5}$$

where N is the number of cylinders unit area (cylinders/m^2), ΔS is the mean space (m) between the cylinders, and d and H are the cylinder diameter (m) and height (m), respectively.

Nepf (1999) defined a dimensionless population density as $ad = d^2 / \Delta S^2$ for a cylindrical model where ad represents the fractional volume of the flow domain occupied by plants.

Windbreak models

Identical cylinders with diameter (d) of 4.0 mm and height (H) of 100 mm were used in the experiment in staggered array configurations. The model was installed in the complete cross-section width of the wind tunnel from wall to wall perpendicular to the wind direction. The experimental apparatus and configuration are shown in Table 1 and Fig. 1.

Table 1. Arrangement of windbreak model and experimental configurations

ad	Relative windbreak width(W/H)					Spacing in cross stream direction，S_t	Spacing in streamwise direction，S_r
0.03	0.20	0.36	0.52	0.68	0.84	8d	4d
0.07	0.14	0.28	0.52	0.88		4d	3.4d

Drag forces were measured in every case, and velocity field were measured when ad=0.03, width 0.2H, 0.84H.

Numerical model and approach

Governing equation

The simulation was based on the Reynolds-averaged Navier-Stokes equation (RANS) using the k-ε turbulence closure model (Launder and Spalding 1974). Four types of equations were solved in each case: continuity equation (6), RANS equation (7), and two turbulence closure equations (8 and 9) for the turbulence kinetic energy (k) and for the dissipation rate of turbulent kinetic energy (ε), respectively.

$$\frac{\partial u_i}{\partial x_i} = 0 \tag{6}$$

$$u_j \frac{\partial u_i}{\partial x_j} = -\frac{1}{\rho}\frac{\partial p}{\partial x_i} + \nu \frac{\partial^2 u_i}{\partial x_j \partial x_j} - \frac{\partial}{\partial x_j}\left(\overline{u_i' u_j'}\right) - C_d a u_i |V| \tag{7}$$

$$u_j \frac{\partial k}{\partial x_j} = \frac{\partial}{\partial x_j}\left[\left(\frac{\nu}{\sigma_k}\right)\frac{\partial k}{\partial x_j}\right] + G_k - \varepsilon + C_d a |V|^3 \tag{8}$$

$$u_j \frac{\partial \varepsilon}{\partial x_j} = \frac{\partial}{\partial x_j}\left[\left(\frac{\nu}{\sigma_\varepsilon}\right)\frac{\partial \varepsilon}{\partial x_j}\right] + C_{\varepsilon 1} G_k \frac{\varepsilon}{k} - C_{\varepsilon 2}\frac{\varepsilon^2}{k} + \frac{3\varepsilon}{2k} C_d a |V|^3 \tag{9}$$

where u_i, u_j are the i, j velocity components, respectively, x_j is the j coordinate, ρ is the air density, G_k is the turbulent kinetic energy production, and $\overline{u_i' u_j'}$ is the Reynolds stress, which can be expressed as:

$$-\overline{u_i' u_j'} = \nu\left(\frac{\partial u_i}{\partial x_j} + \frac{\partial u_j}{\partial x_i}\right) - \frac{2}{3}\delta_{ij} k \tag{10}$$

$$\nu = C_\mu \frac{k^2}{\varepsilon} \tag{11}$$

where ν is the turbulent viscosity, δ_{ij} is the Kronecker delta, σ_k (= 1.0) and σ_ε (= 1.3) are turbulent Prandt numbers for k and ε, respectively, and C_μ, $C_{\varepsilon 1}$, and $C_{\varepsilon 2}$ are model constants (C_μ= 0.09; $C_{\varepsilon 1}$=1.44; $C_{\varepsilon 2}$=1.92; Launder and Spalding 1974). Mean velocity $|V| = \sqrt{(u_j)^2}$.

Boundary conditions

In this paper, the boundary conditions of the computational domain were the inlet boundary conditions used in equation (1). The outlet conditions were the homogeneous Neumann conditions u_x=v_x=0. At the upper and lower faces, the boundary conditions for k, ε and the velocity are wall functions.

Numerical scheme

In this model, the Reynolds-averaged Navier-Stokes equation for an incompressible fluid is solved in a generalized coordinate system. In the present study, the semi-implicit method for pressure-linked equations (SIMPLE) algorithm was used to correct the pressure and velocity, and the governing equations were discretized using the finite volume method.

Average velocity

The averaged wind velocity was calculated as:

$$U_{average} = \frac{1}{H}\int_0^H U(z)dz \tag{12}$$

where $U(z)$ is wind velocity at height z.

Results and discussion

Relationship between drag force and windbreak width

The total drag force acting on the windbreak model as a function of the relative windbreak width (*W*/*H*) is shown in Fig. 2(a). The results show that the total drag force rapidly increased with relative windbreak widths of less than 0.5 and 0.7 in cases of *ad*=0.07 and *ad*=0.03, respectively. As the relative windbreak width increased above those two values, the total drag-force increasing rate became lower. The point at where the total drag-force increasing rate became less, moved in the windbreak downstream direction as the value of *ad* decreases. This may be due to the diminished drag on downstream rows of the windbreak. This result from the downstream cylinders demonstrated a lower impact velocity due to the velocity reduction in the wake by upstream cylinders. In addition, the drag force values increased as the windbreak density increased. The bulk drag coefficient decreased slightly as the width increased (Fig. 2b). The relationship between the bulk drag coefficient C_d and the relative windbreak width (*W*/*H*) can be represented by the following equation, which is derived from the experimental results shown in Fig. 2 as:

$$C_d = k_d(W/H)^{-b} \qquad (13)$$

where k_d, b are constants and depend on the *ad* value as shown in Fig. 2.

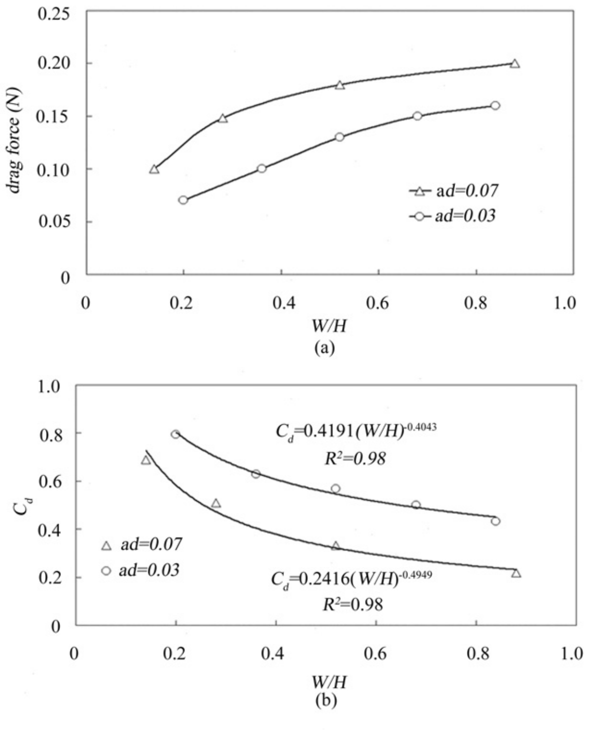

Fig. 2 Drag force characteristics for windbreak models with different widths: (a) total drag force, (b) bulk drag coefficient

Validation of numerical simulation

Before putting any of these modules into application, key issues about them need to be validated and examined to give the best or much better performances. To verify the applicability of the turbulence model and the value of the drag coefficient in the present study, the wind tunnel experimental data were compared with the numerical simulation results.

Fig. 3 shows comparisons of the simulated and measured velocity vertical profiles located at $x = 1$ *H*, 5 *H*, downstream of the windbreak for *ad* = 0.03, when *W*/*H* = 0.2, 0.84. Fig. 4 shows the variation of the horizontal velocity profile along the wind direction at the same height of *z*/*H* (= 0.5) for *ad*=0.03, when *W*/*H* =0.2, 0.84, respectively. As shown in these figures, the simulated wind velocity results accord well with the experimental values.

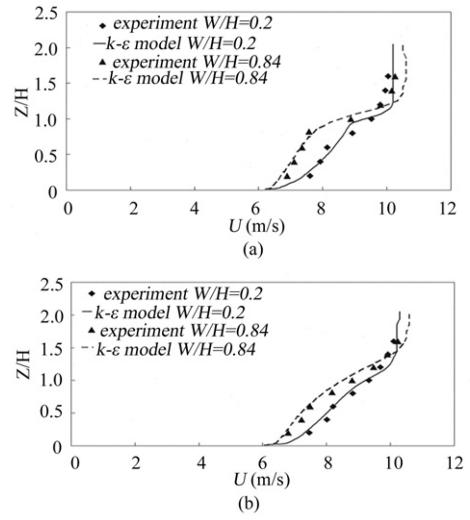

Fig. 3 Vertical profiles of measured wind velocity in comparison with numerical simulation for different streamwise locations: (a) x = 1*H*, (b) x = 5*H*.

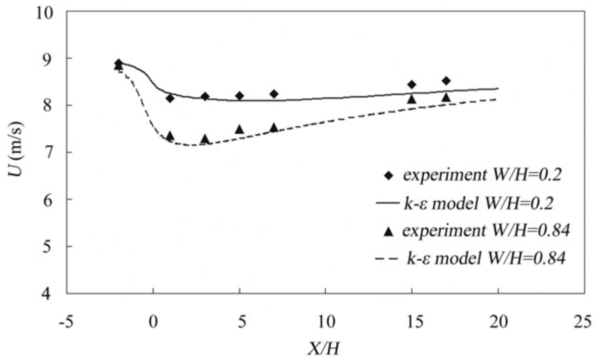

Fig. 4 Horizontal profile of wind velocity at height z = 0.6*H*

Wind velocity profiles and windbreak width

The velocity field was calculated by changing the relative windbreak widths from 0.2 to 8 using the numerical simulation model, to study the effect of windbreak width on the wind velocity reduction behind the windbreak. Characteristics of wind velocity reduction behind the windbreak can be expressed by many parameters. The most commonly used are shelter length (L_{20}), over which wind velocity in the downstream is reduced by 20%, and the wind velocity minimum value (U_{min}) and its location (X_{min}) as shown in Fig. 5.

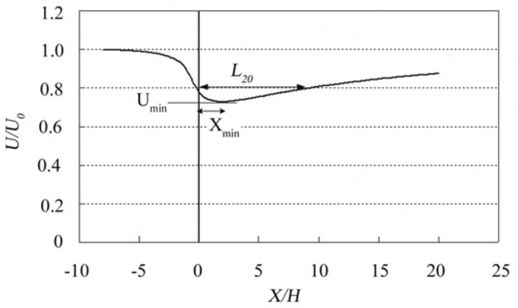

Fig. 5 Definition of characteristic parameters that explain the shelter effect

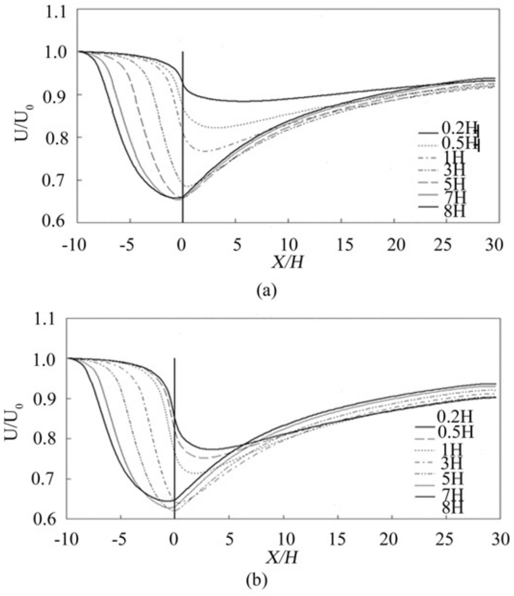

Fig. 6 Horizontal profile of wind velocity for different values of windbreak width at $z = 0.5H$: (a) for *ad*=0.03, (b) for *ad*=0.07

The effects of changes in windbreak width on the wind velocity horizontal profiles are shown in Fig. 6 for different windbreak widths at height 0.5 *H*, and in Fig. 7 for the same widths at height 0.15 *H*, when *ad*=0.03, 0.07, respectively. As the windbreak width increased, the location of the minimum wind velocity (X_{min}) moved toward the windbreak and may move into the wider windbreak (negative X_{min}). With increasing windbreak width, the wind velocity first decreased until it reached its minimum value, and then increased again. When *ad*=0.03, the relative windbreak width value of 7 had the lowest wind velocity value, while for *ad*=0.07, the relative windbreak width value of 5 had the lowest wind velocity value. These results are similar to those of Wang and Takle (1996). However, at the height of 0.15 *H*, the downstream velocity recovered quickly as the windbreak width increased, and the minimum wind velocity (U_{min}) was higher than that at the height of 0.5 *H*. This result differs from that of Wang and Takle (1996).

Fig. 8 shows the relationships between L_{20} and windbreak width for *ad*=0.03 and 0.07, respectively. The results in Fig. 8 show that L_{20} significantly increased until the relative windbreak width was equal to 1 for *ad*=0.07 or to 3 for *ad*=0.03. Furthermore, it decreased slightly as the width increased. It was found that the windbreak widths greatly affected L_{20} values because windbreaks with higher density and narrower width have larger L_{20} values.

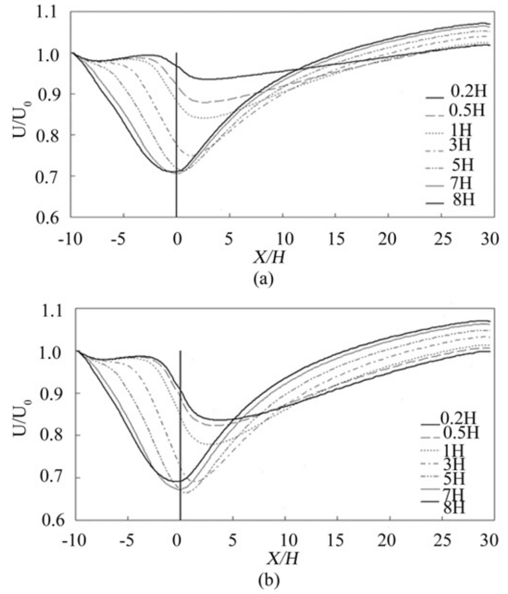

Fig.7 Wind velocity horizontal profiles for different values of windbreak width $z = 0.15H$: (a) for *ad*=0.03, (b) for *ad*=0.07

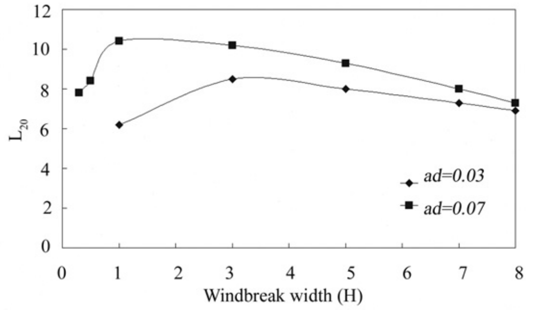

Fig. 8 Values of L_{20} for different windbreak widths.

The average relative velocity values with different windbreak widths in experiments at streamwise locations $x = 10$ *H* and 15 *H* are shown in Fig. 9 (a) and (b), respectively. The results show that at location $x = 10$ *H* the average velocity clearly decreased until the relative windbreak width was equal to 3 for *ad*=0.03, and to 1 for *ad*=0.07, and then slightly increased as the width increased. The windbreak with the relative width of 1 for *ad*=0.07 had the lowest average wind velocity at location x = 10 *H*. Fig. 9(b) clearly shows that the average velocity decreased when the relative windbreak width was less than or equal to 1, and slightly increased as the width increased for both *ad* values (*ad*=0.03 and 0.07).

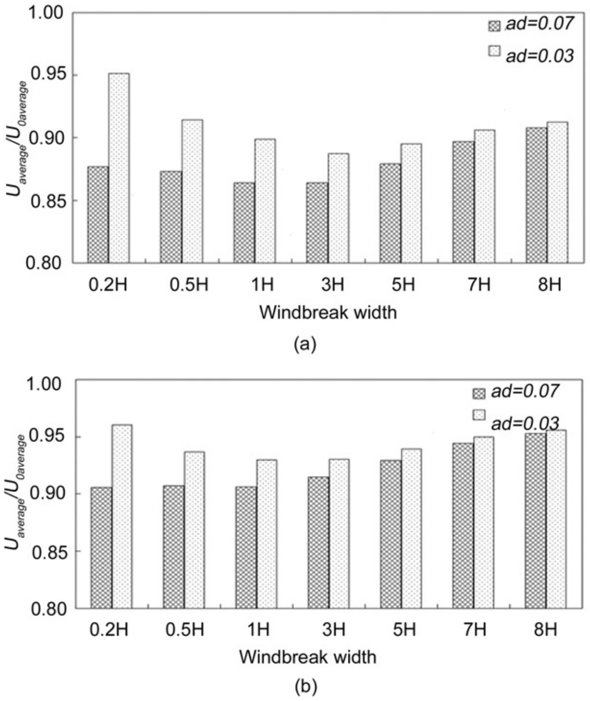

Fig. 9 Relative average velocities for different windbreak widths: (a) location x = 10*H*, (b) location x = 15*H*

Summary and conclusions

The variations of the drag force and the bulk drag coefficient values with different windbreak widths were experimentally determined to investigate the effects of windbreak width on the wind velocity profile behind a windbreak. The variations in the flow with different windbreak widths were also studied numerically. The relationship between the bulk drag force coefficient C_d and the relative windbreak width (W/H) can be presented by the function of $C_d = k_d\ (W/H)^{-b}$. The drag force increased with increased windbreak width, but the increase was not linear because of the sheltering effect. The windbreak width greatly affected the minimum wind velocity and location behind and downstream from the windbreak.

References

Bagnold RA. 1973. *The Physics of Blown Sand and Desert Dunes,* 4th Edition. London: Chapman & Hall.

Bradley EF, Mulhearn PJ. 1983. Development of velocity and shear stress distribution in the wake of a porous shelter fence. *J Wind Eng Ind Aerodyn,* **15**: 145−156.

Cornelis WM, Gabrieis D. 2005. Optimal windbreak design for wind-erosion control. *J Arid Environments*, **61**: 315−332.

Guan DX, Zhang YS, Zhu TY. 2003. A wind-tunnel study of windbreak drag. *Agricultural and Forest Meteorology*, **118**: 75−84.

Guyot G. 1978. Determination des efforts exerces par le vent sur un brise-vent. *Boundary-Layer Meteorology*, **15**: 57−67.

Hagen LJ, Skidmore EL, Miller PL, Kipp JE. 1981. Simulation of effect of wind barriers on airflow. *Trans ASAE*, **24**: 1002−1008.

Heisler GM, DeWalle DR. 1988. Effects of windbreak structure on wind flow. *Agriculture Ecosystems and Environment*, **22-23**: 41−69.

Jenson M. 1958. The model law for phenomena in the natural wind. *Ingeniören*, **2**: 121−128.

Launder BE, Spalding DB. 1974. The numerical computation of turbulent flow. *Computational Methods in Applied Mechanical Engineering*, **3**: 269−289.

Moysey EB, McPherson FB. 1966. Effect of porosity on performance of windbreaks. *Trans ASAE,* **9**: 74−76.

Nepf HM. 1999. Drag, turbulence, and diffusion in flow through emergent vegetation. *Water Resources Research*, **35**(2): 479−489.

Perera MDAS. 1981. Shelter behind two-dimensional solid and porous fences. *J Wind Eng Ind Aerodyn*, **8**: 93−104.

Raine JK, Stevenson DC. 1977. Wind protection by model fence in a simulated atmospheric boundary layer. *J Ind Aerodyn*, **2**: 159−180.

Seginer IDO. 1972. Windbreak drag calculated from the horizontal velocity field. *Boundary-Layer Meteorology*, **3**: 87−97.

Wang H, Takle ES. 1995. A numerical simulation of boundary-layer flows near shelterbelts. *Boundary-Layer Meteorology*, **75**: 141−173.

Wang H, Takle ES. 1996. On three-dimensionality of shelterbelt structure and its influences on shelter effects. *Boundary-Layer Meteorology*, **79**: 83−105.

Wilson JD. 1985. Numerical studies of flow through a windbreak. *J Wind Eng Ind Aerodyn*, **21**: 119−154.

Wilson JD. 1987. On the choice of a windbreak porosity profile. *Boundary-Layer Meteorology*, **38**: 37−49.

Woodruff NP, Fryrear DW, Lyles L. 1963. Engineering simulation and momentum transfer principles applied to shelterbelt studies. *Trans ASAE*, **6** (1): 41−47.